

## Atomically Unveiling an Atlas of Polytypes in Transition-Metal Trihalides

Xiaocang Han,<sup>⊥</sup> Jing-Yang You,<sup>⊥</sup> Shengqiang Wu, Runlai Li, Yuan Ping Feng, Kian Ping Loh,<sup>\*</sup> and Xiaoxu Zhao<sup>\*</sup>Cite This: *J. Am. Chem. Soc.* 2023, 145, 3624–3635

Read Online

ACCESS |



Metrics &amp; More

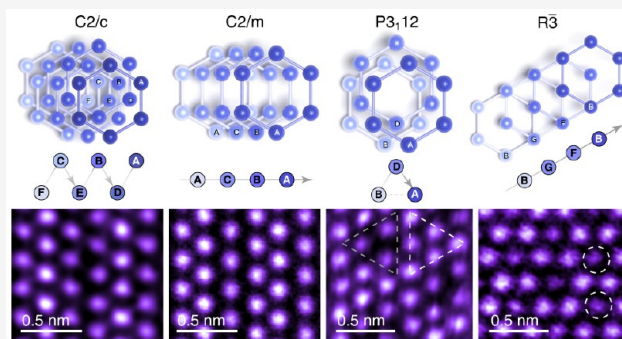


Article Recommendations



Supporting Information

**ABSTRACT:** Transition-metal trihalides  $\text{MX}_3$  ( $\text{M} = \text{Cr}, \text{Ru}$ ;  $\text{X} = \text{Cl}, \text{Br}, \text{and I}$ ) belong to a family of novel two-dimensional (2D) magnets that can exhibit topological magnons and electromagnetic properties, thus affording great promises in next-generation spintronic devices. Rich magnetic ground states observed in the  $\text{MX}_3$  family are believed to be strongly correlated to the signature Kagome lattice and interlayer van der Waals coupling raised from distinct stacking orders. However, the intrinsic air instability of  $\text{MX}_3$  makes their direct atomic-scale analysis challenging. Therefore, information on the stacking-registry-dependent magnetism for  $\text{MX}_3$  remains elusive, which greatly hinders the engineering of desired phases. Here, we report a nondestructive transfer method and successfully realize an intact transfer of bilayer  $\text{MX}_3$ , as evidenced by scanning transmission electron microscopy (STEM). After surveying hundreds of  $\text{MX}_3$  thin flakes, we provide a full spectrum of stacking orders in  $\text{MX}_3$  with atomic precision and calculated their associated magnetic ground states, unveiled by combined STEM and density functional theory (DFT). In addition to well-documented phases, we discover a new monoclinic  $\text{C2}/c$  phase in the antiferromagnetic (AFM) structure widely existing in  $\text{MX}_3$ . Rich stacking polytypes, including  $\text{C2}/c$ ,  $\text{C2}/m$ ,  $\text{R}\bar{3}$ ,  $\text{P3}_112$ , etc., provide rich and distinct magnetic ground states in  $\text{MX}_3$ . Besides, a high density of strain soliton boundaries is consistently found in all  $\text{MX}_3$ , combined with likely inverted structures, allowing AFM to ferromagnetic (FM) transitions in most  $\text{MX}_3$ . Therefore, our study sheds light on the structural basis of diverse magnetic orders in  $\text{MX}_3$ , paving the way for modulating magnetic couplings *via* stacking engineering.



## INTRODUCTION

Since the discovery of intrinsic long-range magnetic order in atomically thin van der Waals (vdW) crystals, two-dimensional (2D) vdW magnetic materials have attracted significant attention for their exceptional performance in magnetic spintronic and magnetoelectric devices.<sup>1–5</sup> Notably,  $\text{MX}_3$  ( $\text{M} = \text{Cr}, \text{Ru}$ ;  $\text{X} = \text{Cl}, \text{Br}, \text{and I}$ ) is a crucial member of 2D magnets with intriguingly tunable magnetic properties,<sup>6</sup> such as large tunneling magnetoresistance,<sup>7,8</sup> spin liquid,<sup>9,10</sup> topological magnons,<sup>11,12</sup> and electron–phonon coupling,<sup>13</sup> which have great prospects in spin-filter magnetic tunnel junction,<sup>14,15</sup> nonvolatile memory,<sup>16</sup> spin valve,<sup>17</sup> and spintronic and magnonic applications.<sup>18</sup>

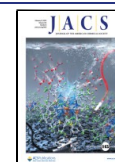
Intrinsically rich magnetic orders inherited in the  $\text{MX}_3$  family can be further precisely modulated by electric gating,<sup>19</sup> pressure,<sup>20</sup> electrostatic doping,<sup>21</sup> stacking registry,<sup>22</sup> etc. The essence of triggering such magnetic order modulation is to change the interlayer vdW coupling.<sup>19–22</sup> In addition to introducing an external force to control the vdW coupling, a more natural and generic way is to create different stacking arrangements *via* interlayer sliding or rotating. For example,

there are two representative phases in  $\text{CrI}_3$ , *i.e.*, antiferromagnetic (AFM) monoclinic (space group  $\text{C2}/m$ ) stacking and ferromagnetic (FM) rhombohedral (space group  $\text{R}\bar{3}$ ) stacking registries.<sup>23</sup> Different FM and AFM magnetic orders have been observed in two phases due to the unique  $\text{M–X–X–M}$  superexchange interaction and spin–lattice coupling stemming from distinct interlayer stacking orders.<sup>23–25</sup> Taking bilayer  $\text{CrBr}_3$  as an example, the interlayer magnetic coupling can be either FM or AFM depending on the stacking order controlled by the interlayer twist angle and in-plane translation.<sup>22</sup> Therefore, stacking engineering has been demonstrated as a promising approach to tuning the magnetic properties of  $\text{MX}_3$ .

Magnetic ground states induced by interlayer gliding have been a core focus of density functional theory (DFT)

Received: December 1, 2022

Published: February 3, 2023



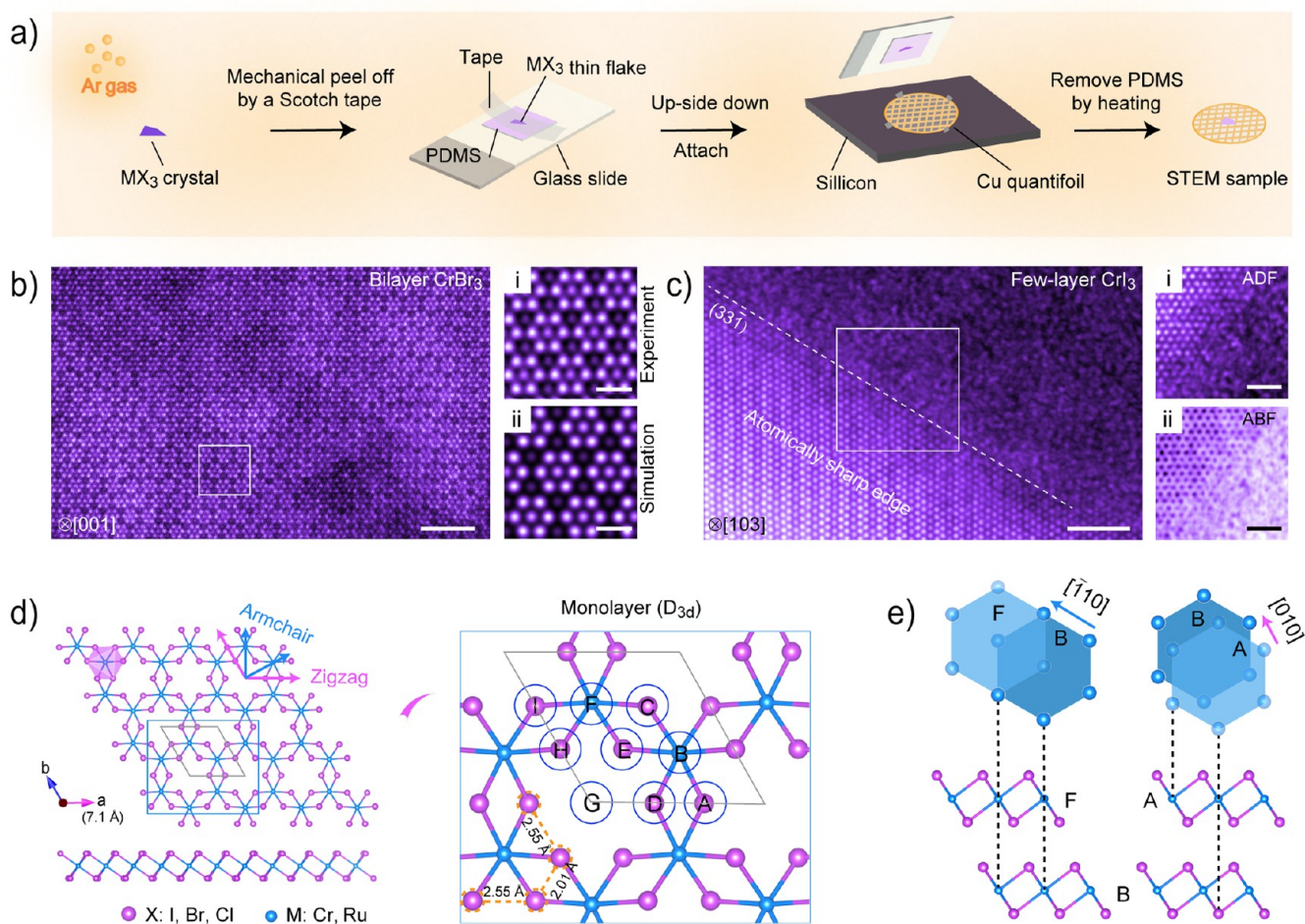


**Figure 1.** Dry transfer method for atomically thin MX<sub>3</sub> flakes. (a) Schematic illustration of the dry transfer method. (b, c) Atomic-resolution ADF-STEM images showing the success of the dry transfer method. The as-transferred bilayer (b) CrBr<sub>3</sub> was confirmed by the consistency of (i) experimental and (ii) simulated images. The as-transferred atomically thin (c) CrI<sub>3</sub> displays a clean and atomically sharp edge in both (i) ADF and (ii) annular bright-field (ABF) imaging. (d) Atomic model of the DFT-optimized monolayer CrI<sub>3</sub>. The top and side views are depicted in the top and bottom panels. An enlarged atomic model showing nine stacking sites for the second layer is depicted in the right panel. The armchair and zigzag directions are labeled by light cyan and purple lines, respectively. (e) Top and side views of bilayer MX<sub>3</sub> in BF [110] and AB [010] stackings. In the top view, iodine atoms are omitted for clarity. Scale bars: (b, c), 2 nm; (b<sup>iii</sup>), 0.5 nm; and (c<sup>iii</sup>), 1 nm.

calculations in MX<sub>3</sub>,<sup>26,27</sup> which is in good agreement with most experimental observations so far.<sup>28</sup> However, less attention has been paid to how the stacking order affects magnetic properties in 2D few-layer MX<sub>3</sub>. The lack of knowledge on the various polymorphs and polytypes of MX<sub>3</sub> stems partly from the poor stability of MX<sub>3</sub>, where rapid sample degradation in air precludes microscopic characterization.<sup>29</sup> Despite the absence of phase transition occurring in atomically thin CrI<sub>3</sub> as verified by electron microscopy,<sup>30</sup> intriguing AFM to FM magnetic orders have been widely observed.<sup>2,20,31</sup> The origin of the different (AFM/FM) magnetic ground states of CrI<sub>3</sub> thin films remains elusive. Given a rich interplay between stacking order and interlayer exchange,<sup>26,32,33</sup> the atomic-scale stacking features and associated magnetic profiles are interesting subjects to be investigated in few-layer MX<sub>3</sub> crystals.

The layered vdW materials, MX<sub>3</sub>, are a three-atom-thick sandwich-like structure analogous to 1T-phase MoS<sub>2</sub>. The key difference from 1T-MoS<sub>2</sub> is that the sandwiched M metal layer only occupies octahedral vacancies with 66.7% occupancies created by two layers of X planes, exhibiting orderly  $\sqrt{3}a \times \sqrt{3}a$  periodic metal vacancies. The structure is endowed with

rich stacking polytype chemistry that differs in stacking arrangements of neighboring MX<sub>3</sub> slabs along the crystallographic *c* axis. Bulk chromium trihalides CrX<sub>3</sub> (X = Cl, Br, and I) are suggested to undergo temperature-dependent crystallographic phase transitions, from high-temperature monoclinic C2/*m* stacking to low-temperature rhombohedral R $\bar{3}$  phase with neglectable (significant) change in the intralayer (interlayer) structure<sup>23,34–36</sup> as verified by X-ray diffraction and the theory.<sup>23</sup> The phase transition takes place near 240, 420, and 210 K in bulk CrX<sub>3</sub> (X = Cl, Br, and I), respectively,<sup>36</sup> which was not observed in few-layer CrX<sub>3</sub>.<sup>30,37</sup> The layered RuCl<sub>3</sub> compounds have been reported to adopt the monoclinic C2/*m* phase<sup>38</sup> at low temperatures with a zigzag AFM structure and exhibit the trigonal P3<sub>1</sub>12 phase at high temperatures.<sup>39</sup> Given the weak interlayer vdW coupling,<sup>2</sup> there is a tendency to form stacking faults and metastable polytypes, owing to their very similar formation energies with the normal phase.<sup>10,40</sup> Other than the most commonly observed C2/*m* and R $\bar{3}$  phases, other interesting stacking polytypes with intriguing physical properties remain to be explored. In addition, most of the recently reported MX<sub>3</sub> suffer



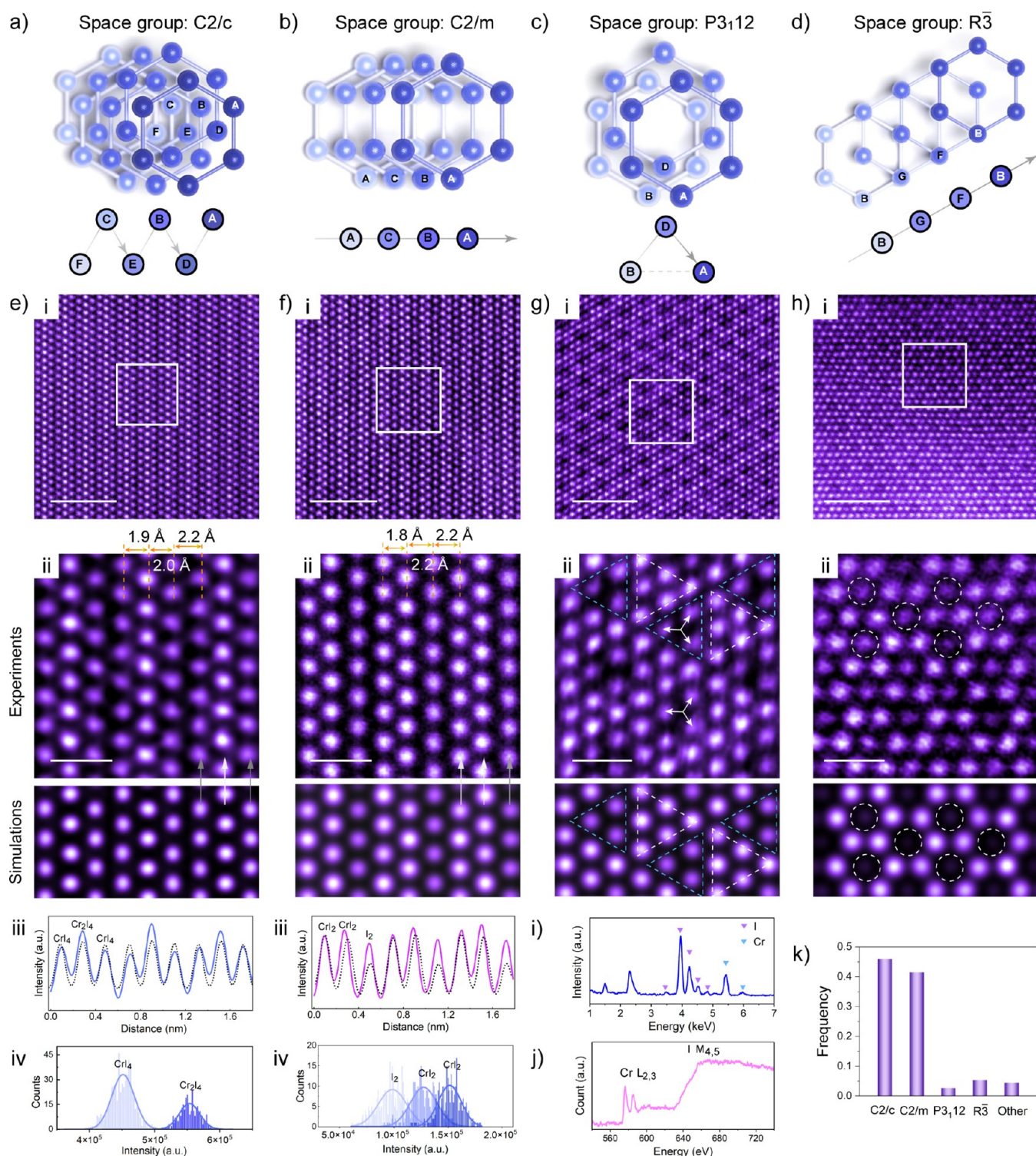


**Figure 2.** Atomic structures of various stacking polytypes of  $\text{CrI}_3$ . The atomic models of layered  $\text{CrI}_3$  viewed along the  $c$  axis in (a)  $\text{C2/c}$ , (b)  $\text{C2/m}$ , (c)  $\text{P3}_112$ , and (d)  $\text{R}\bar{3}$  phases. For clarity, the Cr atoms in different layers are shown by different colors ( $\text{I}^-$  ions are omitted for clarity). (e–h) Top (i), atomic-resolution ADF-STEM images showing different stacking polytypes of few-layer  $\text{CrI}_3$  crystals consisting of  $\text{C2/c}$ ,  $\text{C2/m}$ ,  $\text{P3}_112$ , and  $\text{R}\bar{3}$  phases from left to right, respectively; middle (ii), the zoom-in images from white regions in panel (i) and corresponding simulated images; and bottom (iii, iv), (iii) the averaged intensity of all atomic sites and (iv) statistical analysis of intensity from experimental images of  $\text{C2/c}$  and  $\text{C2/m}$  in panels (e) and (f). The simulated intensity line profiles (labeled by a black dotted line) are presented for comparison. (i, j) Energy-dispersive X-ray spectroscopy (EDS) and electron energy loss (EEL) spectra of core-level edges of  $\text{CrI}_3$  thin film. (k) Frequency of different stacking structures, including  $\text{C2/c}$ ,  $\text{C2/m}$ ,  $\text{P3}_112$ ,  $\text{R}\bar{3}$  and other stackings, after counting over one hundred flakes. The white arrows indicated the displacement of iodine columns in panel (g). Scale bars: (e–h)<sup>i</sup>, 2 nm and (e–h)<sup>ii</sup>, 0.5 nm.

from a fundamental obstacle, *i.e.*, instability under air conditions, which severely hinders the structural characterization of  $\text{MX}_3$  with atomic precision.<sup>41</sup>

Here, we employed a completely dry transfer method to transfer atomically thin  $\text{MX}_3$  crystals (Figure S1) for atomic-scale observations inside the glovebox. Using atomic-resolution annular dark-field scanning transmission electron microscopy (ADF-STEM) and image simulation, an atlas of stacking polytypes, including the newly discovered  $\text{C2}/c$  phase, has been atomically identified, and their associated magnetic orders are further predicted by DFT calculations. The  $\text{C2}/c$  monoclinic stacking has similar formation energy with  $\text{C2}/m$  in the few-layer  $\text{CrI}_3$  and coexist, whereas  $\text{P3}_112$  and  $\text{R}\bar{3}$  phases are less common. Analogous to the  $\text{C2}/m$  phase, the  $\text{C2}/c$  polytypes reveal an AFM structure, whereas their reversed structures and strain soliton boundaries consistently found in all  $\text{MX}_3$  allow the AFM to FM transitions in most  $\text{MX}_3$ . On the other hand,  $\text{P3}_112$  and  $\text{R}\bar{3}$  phases illustrate distinct magnetic couplings in different  $\text{MX}_3$ . After counting over one hundred crystals, we found that different  $\text{MX}_3$  exhibit unique stacking polytype distributions, paving an alternative way to design spintronic devices with desirable magnetic properties by switching the stacking structures in the same vdW 2D magnet.

## RESULTS AND DISCUSSION

The dry-stamp transfer method was employed to produce atomically thin and clean 2D flakes suitable for atomic-resolution STEM imaging,<sup>42</sup> especially for the  $\text{MX}_3$  crystals sensitive to air, light, and/or moisture. As illustrated in Figure 1a, the mechanically exfoliated thick  $\text{MX}_3$  flakes prepared in an inert argon glovebox were further exfoliated by poly-(dimethylsiloxane) (PDMS) and then dry transferred onto a targeted Cu Quantifoil grid after removing PDMS by mild heating, leaving few-layer flakes suspended over the holes of the support STEM grid. Figure 1b shows the atomic-scale STEM images of successfully transferred  $\text{CrBr}_3$ , where the local thickness is down to bilayers, as corroborated by the simulated image (Figure S2). This dry transfer method also applies to the air-sensitive  $\text{CrI}_3$ . It can be seen that the atomic structure of the  $\text{CrI}_3$  flake remains intact and homogeneous even along the edge region without substantial degradation (Figure 1c). Interestingly, the atomically sharp edge is highly faceted, preferring to terminate along the  $\{3\bar{3}1\}$  planes of the crystal (Figure 1c). In 2D layered  $\text{MX}_3$ , similar to the structure of  $\text{CrI}_3$  (Figure 1d), the M ions in each layer are arranged in a honeycomb network with distorted edge-sharing octahedral coordination by six X ions. On the basis of the atomic structure of monolayer  $\text{MX}_3$  (point group,  $D_{3d}$ ), there are nine possible interlayer stacking sites per unit cell if only staggered or eclipsed configurations were considered, *i.e.*, labeled by A, B, C, D, E, F, G, H, and I (Figure 1d, right panel), so that the M in the top layer could be directly stacked over the center of a hole (G), two Cr (B, F), or six X (A, C, D, E, H, I) positions in the bottom layer. The basis vectors *a* and *b* (purple lines) are along the zigzag directions, whereas the armchair directions are marked by cyan lines in the monolayer framework (Figure 1d, left panel). Beyond the monolayer, the stacking phases of layered  $\text{MX}_3$  involve interlayer gliding to change their relative positions upon stacking sequences (Figure 1e), *e.g.*, AB (zigzag direction  $[010]$ ) or BF (armchair direction  $[\bar{1}10]$ ).

To unravel the atomic structure of stacking polytypes in few-layer  $\text{MX}_3$  crystals, an aberration-corrected ADF-STEM was employed to characterize the as-transferred atomically thin

$\text{MX}_3$  samples. Representative atomic-resolution ADF-STEM images of  $\text{CrI}_3$  taken along the *c* axis at room temperature are illustrated in Figure 2e–h. The intensity of an atomic column in ADF-STEM images is roughly proportional to  $\sim Z^{1.6-1.9}$ , where *Z* denotes the atomic number.<sup>43,44</sup> The periodic intensity variations in these STEM images indicate different ordering sequences. Therefore, based on different projected 2D intensity maps shown in ADF-STEM images (Figure 2e–h), the crystal structures of atomically thin  $\text{CrI}_3$  can be unambiguously classified into four distinct stacking types: (1) the  $\text{C2}/m$  monoclinic stacking, (2) the  $\text{C2}/c$  monoclinic stacking, (3) the  $\text{P3}_112$  trigonal stacking, and (4) the  $\text{R}\bar{3}$  rhombohedral phase. The layer arrangements of the Cr framework for the four phases within one period are shown in Figure 2a–d. The atomic-level consistency between the experimental image and its simulation (Figure 2e–h) derived from the DFT-optimized structural models of  $\text{CrI}_3$  unambiguously demonstrates that the ADF-STEM is reliable for directly differentiating the polytypes and local topological defects in 2D materials.

**Atomic-Level Phase Identifications.** As reported by McGuire,<sup>23</sup> there are two representative phases in bulk  $\text{CrI}_3$ , *i.e.*, rhombohedral ( $\text{R}\bar{3}$ ) and monoclinic ( $\text{C2}/m$ ) phases. The  $\text{C2}/m$  monoclinic (ABC) stacking can be uniquely identified by the top-view atomic-resolution images revealing a signature stripy pattern in which each layer glides sequentially along the zigzag direction by  $1/3a$  fractional unit cell (Figure 2b). The well-defined striped topology can be directly visualized by STEM images exhibiting a triple-stripped structure. The lattice arrangements of the  $\text{C2}/c$  phase (Figure 2e<sup>i</sup>) display a triple stripe in which the center line is a bright line and the other two lines are relatively weaker (Figure 2e<sup>ii</sup>). The situation, however, is different in the  $\text{C2}/m$  structure (Figure 2f), where every third line is substantially darker than the other two (Figure 2f<sup>i</sup>).<sup>29,45</sup> It is worth noting that in  $\text{C2}/m$ , the darker line contains only  $\text{I}_2$  hollow atomic columns and the two bright lines are composed of mixed Cr– $\text{I}_2$  (Figure S3). The intensity variation and periodic ordering can be seen clearly in the intensity line profiles (Figure 2e<sup>iii</sup>, f<sup>iii</sup>). These contrast variations can be well explained by the stacking differences between the two phases. Notably, the striped patterns can be observed in almost all  $\text{CrI}_3$  few-layers in this study (Figure 2k), indicating that it is the energetically preferred phase, which is consistent with our calculations in the later section. To the best of our knowledge, the specific structural periodicity of the monoclinic  $\text{C2}/c$  phase in  $\text{CrI}_3$  has not been observed in either exfoliated or chemically produced  $\text{MX}_3$  materials before.

To precisely distinguish the stacking difference between these two monoclinic phases, we statistically analyzed the intensity of all atom sites in STEM images (Figure S4). The corresponding histograms of the intensity distribution of two monoclinic structures are shown in Figure 2e<sup>iv</sup>, f<sup>iv</sup>, respectively. Notably, the intensity distribution is divided into three peaks in  $\text{C2}/m$  (Figure 2f<sup>v</sup>), whereas there are only two significant peaks in  $\text{C2}/c$  stacking (Figure 2e<sup>v</sup>). Based on the *Z*-contrast ADF-STEM image, we can deduce that the striped structure shown in Figure 2e exhibits a  $\text{C2}/c$  monoclinic stacking, confirmed by the simulated image (Figure 2e<sup>ii</sup>, bottom panel). The  $\text{C2}/c$  three-step staircase pattern contains six layers in one unit cell, which can be decomposed into the zigzag stacks of –A–D–B–E–C–F– as illustrated in the atomic model (Figure 2a). The regular intensity feature (Figure 2e<sup>iv</sup>) suggests that the stacking sequence of  $\text{C2}/c$  is definite, otherwise it will



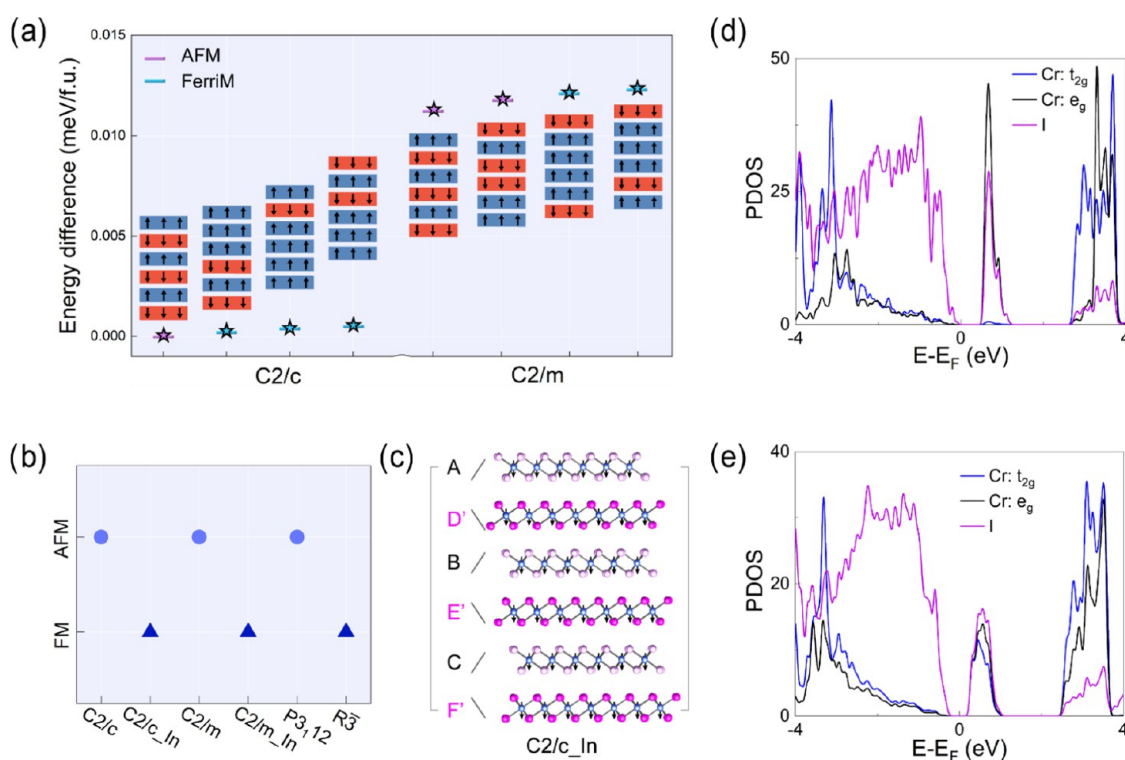


**Figure 3.** Electronic structures of various stacking polytypes of CrI<sub>3</sub>. (a) Relative total energy of the C2/c and C2/m structure with different magnetic configurations, with respect to the C2/c ground state. The magnetization directions along the *c* axis are indicated by black arrows with blue (spin up) and red (spin down) background. (b) Calculated magnetic ground state of different stacking polytypes. (c) Side view of inversion structures of C2/c, denoted as C2/c<sub>In</sub>. Inversion stacking arrangements are created by switching the two iodine atomic layers upside down in one sandwich unit cell (intralayer polymorph). (d and e) Corresponding partial density of states (PDOS) for the ground state of (d) C2/c and (e) C2/c<sub>In</sub>. The PDOS of each orbital channel is represented by different colors as denoted in panels (d) and (e).

result in an irregular image contrast since the layer number is changeable. The stacking of  $-D-$ ,  $-E-$ ,  $-F-$  is similar to  $-A-$ ,  $-B-$ ,  $-C-$ , but they glide relatively along the other degenerate zigzag direction by  $1/3a$  fractional unit cell (Figure 2a). The stripe contrast in C2/c is caused by the alignment of Cr–I<sub>2</sub> positioned on the Cr–I<sub>2</sub> (bright stripes) or I<sub>2</sub> hollow (dark stripes) sites in adjacent layers, as indicated by {Cr<sub>2</sub>I<sub>4</sub>} and {CrI<sub>4</sub>}, respectively. The frequency of bright spots caused by additional Cr atoms is statistically half the frequency of dark spots in the lattice, indexing the stoichiometric ratio of CrI<sub>3</sub>. Besides, the simulated intensity line profiles (Figure 2e<sup>iii</sup>) agree well with the experimental results, reconfirming the C2/c stacking sequence.

In addition, a structural distortion induced by the periodic in-plane Cr–I bond contraction and elongation from ideal monoclinic symmetry (*i.e.*, undistorted CrI<sub>6</sub> octahedron) was observed in multilayer C2/c and C2/m crystals (Figure 2e<sup>ii</sup>, f<sup>ii</sup>). Two bright CrI<sub>2</sub> mixed lines keep away from the dark I<sub>2</sub> line (2.2 Å) in C2/m, while the columns of {CrI<sub>4</sub>} dark lines move toward the bright {Cr<sub>2</sub>I<sub>4</sub>} column lines (1.9 Å) in C2/c. The resulting deviation of the Cr–I bonds leads to a distorted octahedral symmetry, which was further corroborated by the DFT-optimized structure, and is robust against the stacking registry and interlayer coupling (Figures S5 and S6). Furthermore, the observation of the monoclinic phases with lattice distortion suggests real-space atomic-level evidence for distorted octahedra in MX<sub>3</sub>, which is vital to the resultant magnetic ground state due to its high sensitivity to the local geometry.<sup>39,46</sup>

Besides monoclinic phases, we also found the R $\bar{3}$  (Figure 2d, BFG) rhombohedral stacking (Figure 2h<sup>i</sup>), commonly denoted as a low-temperature phase, and it only exists as a tiny fraction ( $\sim 5\%$ ) after counting over one hundred atomically thin CrI<sub>3</sub> flakes (Figure 2k). As shown in Figure 2h<sup>ii</sup>, the atom arrangements of R $\bar{3}$  phase illustrate signature hexagon-shaped periodic bright spots with one dark spot in the middle of a hexagon, confirmed by the consistency with the simulated image (Figure 2h<sup>ii</sup>, bottom panel). The low population of the R $\bar{3}$  phase suggests that it is not energetically favorable at room temperature. Interestingly, an unusual periodic structure, different from the abovementioned rhombohedral and monoclinic stackings, can be observed in few-layer CrI<sub>3</sub> (Figure 2g<sup>i</sup>). The periodic structure (Figure 2g<sup>ii</sup>) consists of a repetition of one unit cell containing six bright spots (marked by a white dashed line) and three less bright spots (marked by a yellow dashed line), similar to the observed P312 phase in an  $\alpha$ -RuCl<sub>3</sub> thin film.<sup>39</sup> Besides, the simulated image (Figure 2g<sup>ii</sup>, bottom panel) from the P312 atomic model agrees well with the experimental results, confirming the P312 (Figure 2c, ABD) stacking sequence. As expected, the bright spots are assigned to Cr–I<sub>2</sub> atomic columns, while the dark one is I<sub>2</sub> hollow atomic columns, producing a specific repeating pattern in P312 trigonal symmetry. In addition, a relative displacement (7.2%) marked by white arrows was observed in the positions of iodine columns, consistent with previous reports in  $\alpha$ -RuCl<sub>3</sub>.<sup>39</sup> The energy-dispersive X-ray spectroscopy (EDS) and electron energy loss spectroscopy (EELS) verified that the as-exfoliated atomically thin CrI<sub>3</sub> flakes were purely composed

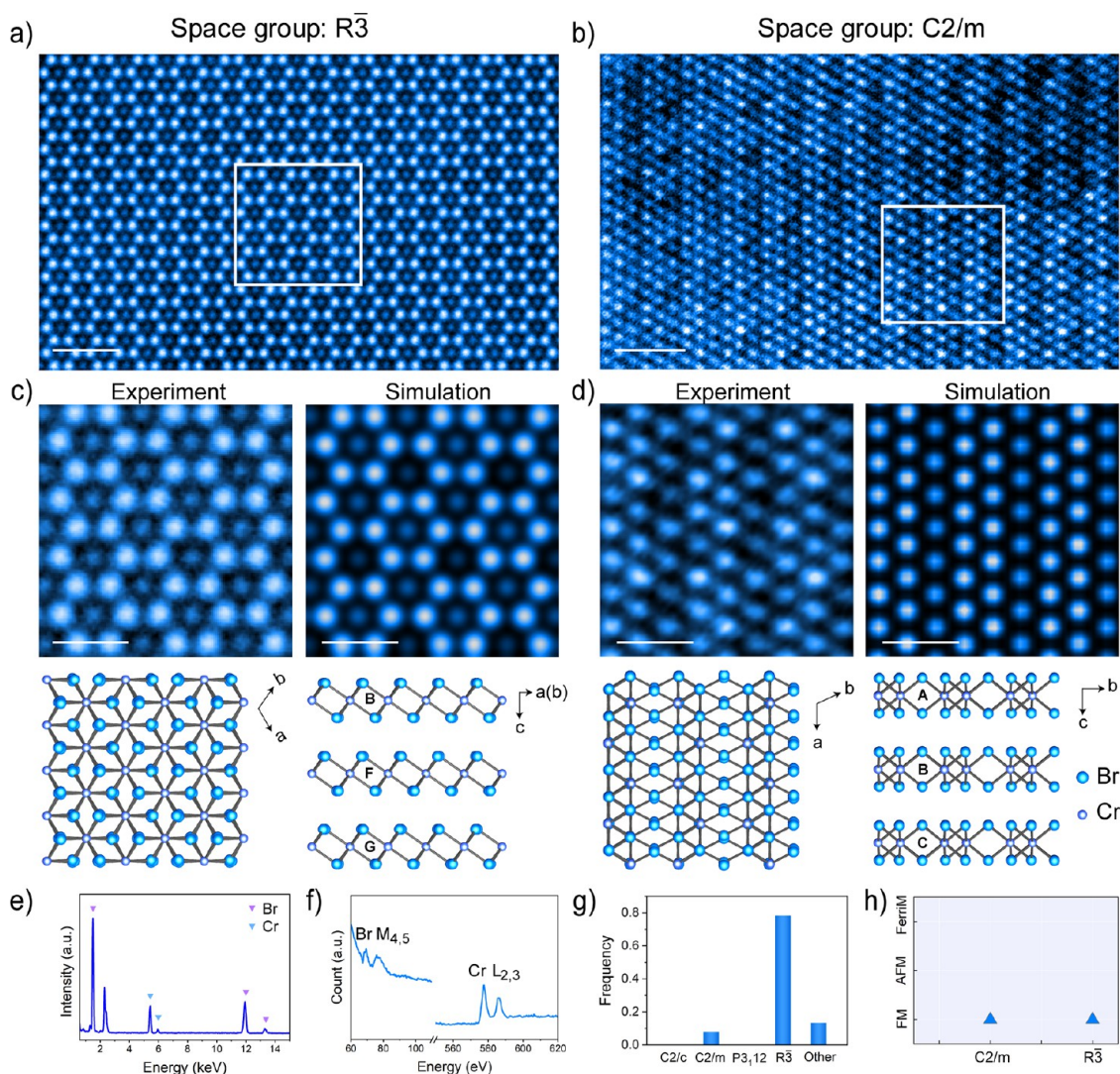


**Figure 4.** Atomic structures of various stacking polytypes of CrBr<sub>3</sub>. (a, b) Atomic-resolution ADF-STEM images showing the (a) R $\bar{3}$  and (b) C2/m stacking polytypes in few-layer CrBr<sub>3</sub> crystals. (c, d) Left, enlarged STEM images corresponding to the regions highlighted with white boxes in panels (a) and (b), respectively, and right, the corresponding simulated images. (e) EDS and (f) EEL spectra of core-level edges of CrBr<sub>3</sub> thin film. (g) Frequency and (h) calculated magnetic ground state of different stacking polytypes. Scale bars: (a, b), 2 nm and (c, d), 0.5 nm.

of Cr and I, with the chemical stoichiometry agreeing very well with MX<sub>3</sub> (Figure 2i,j).

Indeed, the C2/m, C2/c, P3<sub>1</sub>2, and R $\bar{3}$  phases are unique stacking polytypes of CrI<sub>3</sub> arising from distinct interlayer sliding. In C2/m, C2/c, and P3<sub>1</sub>2 stacking registries, one unit layer is collectively translated by  $1/3a$  along the zigzag directions relative to its neighboring layers. On the other hand, adjacent two layers slide relatively for  $\frac{1}{\sqrt{3}}a$  along the armchair direction in the R $\bar{3}$  phase. Across from the edge few-layer regions to the interior thick domains, the 2D CrI<sub>3</sub> flakes may be subject to interlayer gliding to modify its stacking sequence (Figure S1).<sup>45</sup> Collectively, after surveying over one hundred few-layer crystals, we confirm that the C2/c (~46%) and C2/m (~41%) have much higher frequencies in the few-layer CrI<sub>3</sub> system as shown in the statistical counting (Figure 2k), whereas other stacking polytypes including P3<sub>1</sub>2 and R $\bar{3}$  only account for 13%. Therefore, the magnetic properties of few-layer CrI<sub>3</sub> are predominantly determined by C2/c and C2/m phases.

### Magnetic Properties of Various Stacking Polytypes.

To investigate the stacking order-dependent magnetic properties, we carried out first-principles DFT calculations to predict all available magnetic ground states in four different stacking registries. Our results show that the magnetic order of the C2/m, C2/c, and P3<sub>1</sub>2 structures is consistently AFM, while that of R $\bar{3}$  is FM (Figure 3b). These results are in good agreement with the previously reported results, *i.e.*, sliding along the zigzag direction tends to interlayer AFM coupling, while translating along the armchair direction favors FM coupling.<sup>47</sup> Specifically, we focused on monoclinic stackings of C2/m and C2/c, since the monoclinic stackings are ubiquitous in as-exfoliated few-layer CrI<sub>3</sub>, and the rhombohedral stacking is rare (Figure 2k). The relative total energy difference between the magnetic configurations in C2/c and C2/m stackings, with respect to the C2/c ground state, is illustrated in Figure 3a. The magnetization directions are indicated by the black arrows. We found that the C2/c phase with AFM magnetic configuration (three up and three down) is at the energy minimum (Figure S7), consistent with the experimentally observed C2/c structures with the largest proportion. Since STEM imaging is projecting



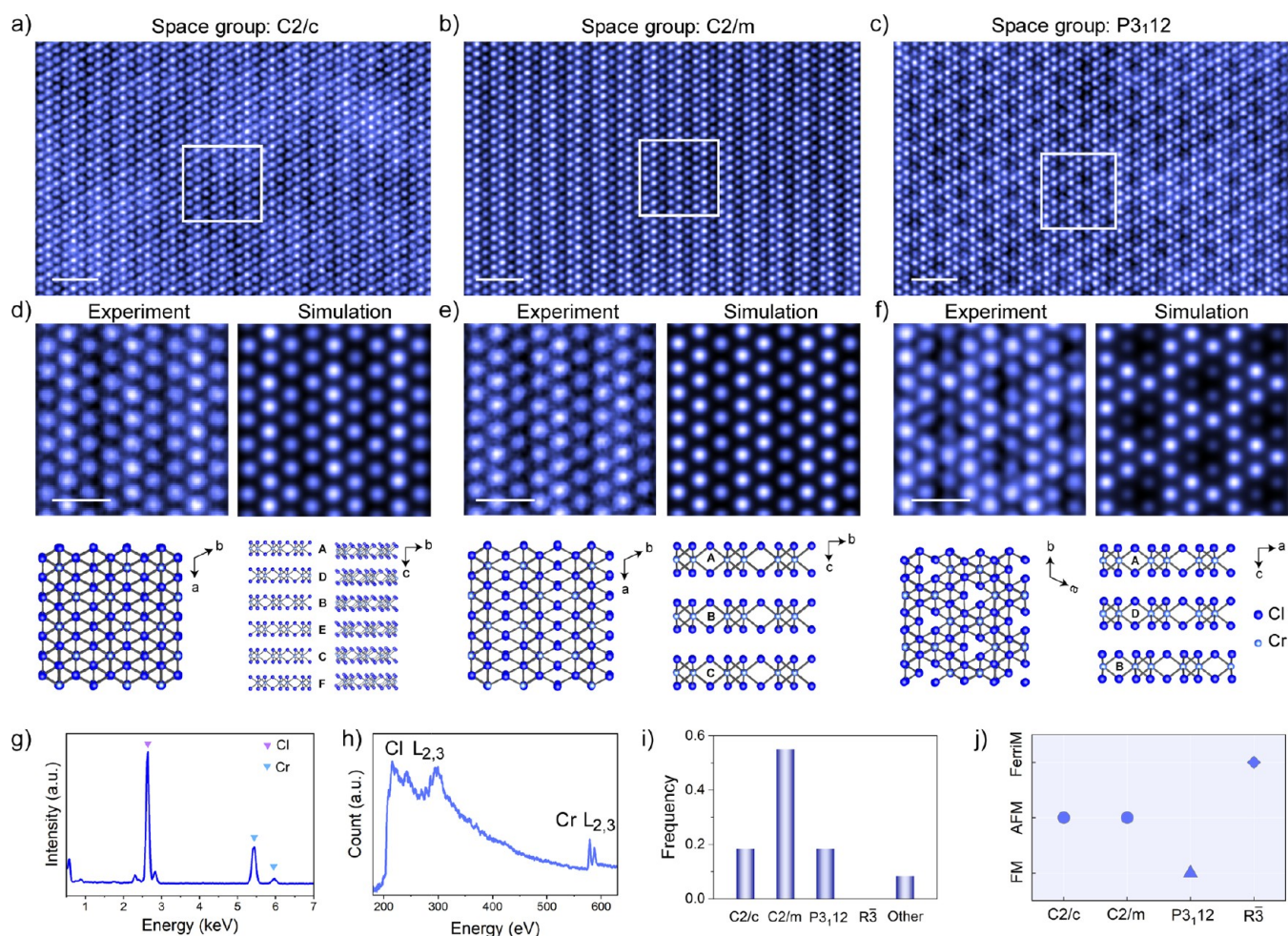


**Figure 5.** Atomic structures of various stacking polytypes of CrCl<sub>3</sub>. (a–c) Atomic-resolution ADF-STEM images showing different stacking polytypes of few-layer CrCl<sub>3</sub> crystals, consisting of C2/c, C2/m, and P3<sub>12</sub> phases from left to right, respectively. (d–f) Left, enlarged STEM images corresponding to the regions highlighted with white boxes in panels (a)–(c), respectively, and right, the corresponding simulated images. (g) EDS and (h) EEL spectra of core-level edges of the CrCl<sub>3</sub> thin film. (i) Frequency and (j) calculated magnetic ground state of different stacking polytypes. Scale bars: (a–c), 2 nm and (d–f), 0.5 nm.

a three-dimensional (3D) crystal into a 2D plane with limited resolution perpendicular to the zone axis, we do not know the exact intralayer stacking order of a single layer MX<sub>3</sub>, e.g., either A-abc or its reversal A'-cba stacking sequence (Figure S8). The uncertainty of such stacking order is a common phenomenon in 2D materials,<sup>22,48</sup> and their consequences on interlayer magnetic interactions have not been well elucidated. To analyze the consequences of such a scenario, we constructed C2/m and C2/c inversion polytypes with inverse intralayer stacking of two iodine atomic planes at the second, fourth, and sixth layers and investigated their magnetic configurations, as depicted in Figures 3b,c and S8. The energy difference between inversion structures and the C2/c ground state is relatively small about 0.014 meV per formula unit (f.u.), implying a significant probability of its presence in CrI<sub>3</sub> (Figure S9). Surprisingly, the inversion structures tend to be FM interlayer coupling, consistent with the calculation in bilayer CrI<sub>3</sub>.<sup>48</sup> Besides, combined with interlayer gliding-induced R $\bar{3}$  and other stacking polytypes along the armchair direction, inversion types indicate a strong FM coupling in the CrI<sub>3</sub> thin film as observed experimentally, which are potential origins for the mysterious FM order observed in bulk CrI<sub>3</sub> crystals (Figure S10).

We now elucidate the stacking-dependent electronic structures of the C2/c and C2/m phases (Figures 3d and S11). We note that band structures and partial density of states (PDOS) distribution of C2/c and C2/m are similar, reflecting their nearly equivalent stacking modes gliding 1/3a along zigzag directions if ignoring the changes of iodine atoms. For each layer, the local magnetic moment is attributed to the half-occupied t<sub>2g</sub> orbital. However, the adjacent layers alternatively occupy the spin-majority and spin-minority t<sub>2g</sub> orbital, resulting in the disappearance of the net magnetic moment. The band structures and PDOS for inversion C2/c and C2/m are plotted in Figures 3e and S12. Compared to the C2/c and C2/m phases with an AFM ground state (Figure S11), the band splitting of the inversion phases is greater due to the severe breaking of parity–time symmetry in ferromagnets. Our calculation results also show that the magnetic moments of adjacent layers in the inversion phases slightly alternate, which is different from those in the C2/c and C2/m phases with the same absolute value, reflecting the influence of different interlayer superexchanges on magnetism. In addition, from the PDOS in Figures 3e and S12, it can be seen that there are additional t<sub>2g</sub> orbitals at 0.5 eV above the Fermi level, and the enhanced t<sub>2g</sub>–e<sub>g</sub> interactions favor the interlayer FM coupling.



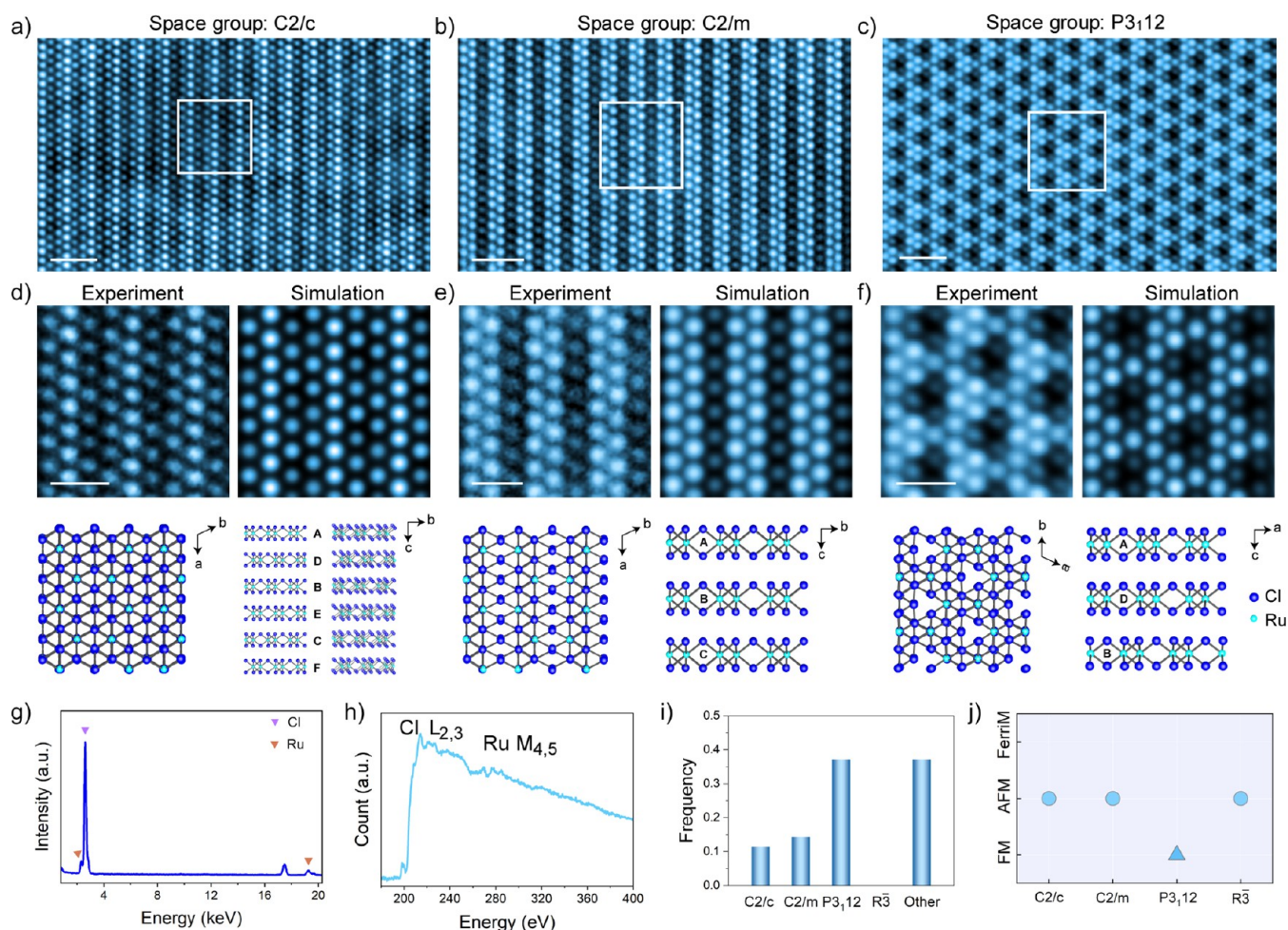


**Figure 6.** Atomic structures of various stacking polytypes of  $\alpha$ -RuCl<sub>3</sub>. (a–c) Atomic-resolution ADF-STEM images showing different stacking polytypes of few-layer  $\alpha$ -RuCl<sub>3</sub> crystals, consisting of C2/c, C2/m, and P3<sub>1</sub>12 phases from left to right, respectively. (d–f) Left, enlarged STEM images corresponding to the regions highlighted with white boxes in panels (a)–(c), respectively, and right, the corresponding simulated images. (g) EDS and (h) EEL spectra of core-level edges of the  $\alpha$ -RuCl<sub>3</sub> thin film. (i) Frequency and (j) calculated magnetic ground state of different stacking polytypes. Scale bars: (a–c), 2 nm and (d–f), 0.5 nm.

**Table 1. Summary of Stacking Structures and Correlated Magnetic Ground States<sup>a</sup>**

Phases	C2/m	R $\bar{3}$	C2/c	P3 <sub>1</sub> 12	C2/m_In	C2/c_In
CrI <sub>3</sub>	AFM	FM	AFM	AFM	FM	FM
CrBr <sub>3</sub>	FM	FM	/	/	/	/
CrCl <sub>3</sub>	AFM	FerriM	AFM	FM	FM	FM
RuCl <sub>3</sub>	AFM	AFM	AFM	FM	FerriM	FerriM

<sup>a</sup>The dominant phases in MX<sub>3</sub> are indicated by green.

**Rich Stacking Polytypes in Various MX<sub>3</sub>.** Rich stacking polytypes are consistently found in other layered chromium trihalides (CrX<sub>3</sub>, X = Cl, Br, and I), as the entire family of CrX<sub>3</sub> possesses an identical basic layer structure together with relatively strong (weak) in-plane (out-of-plane) exchange couplings. Since the compositions and magnetic properties of CrX<sub>3</sub> are different, the stacking registries in CrX<sub>3</sub> are diverse and highly variable. Experimentally, only two stacking orders, *i.e.*, R $\bar{3}$  (Figure 4a,c) and C2/m (Figure 4b,d), exist in few-layer CrBr<sub>3</sub>. The elementary composition was verified by EDS and

EELS (Figure 4e,f). Our atomic-resolution ADF-STEM imaging confirms that the proportion of rhombohedral stacking in the CrBr<sub>3</sub> samples is more than 80% (Figure 4g), consistent with previous observations.<sup>29</sup> Regardless of the stacking orders, both C2/m and R $\bar{3}$  phases in the CrBr<sub>3</sub> illustrate FM interlayer coupling as suggested by the theory (Figure 4h).

In fact, C2/c (Figure 5a,d), C2/m (Figure 5b,e), and P3<sub>1</sub>12 (Figure 5c,f) polytypes showing different interlayer couplings (Figure 5j) also exist widely in CrCl<sub>3</sub> but are different from



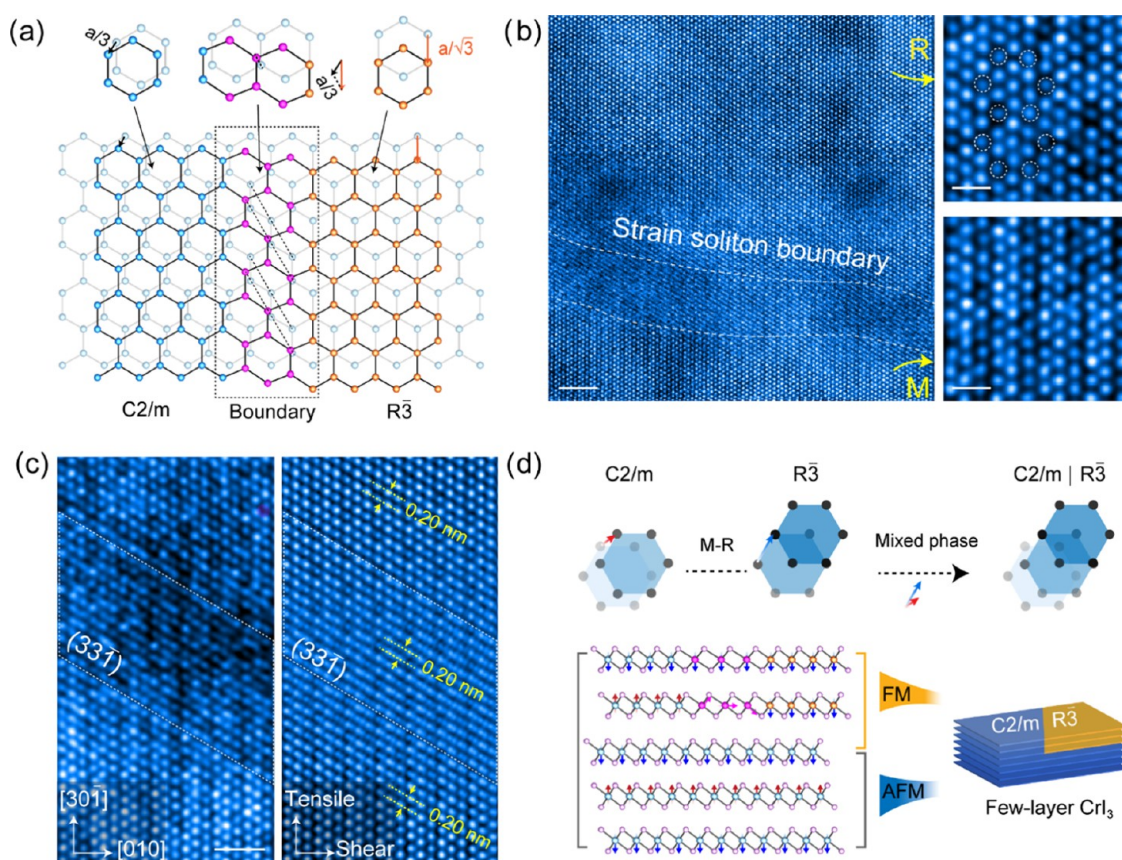


**Figure 7.** Strain soliton boundaries in few-layer  $\text{CrI}_3$ . Atomic-resolution ADF-STEM images of monoclinic–rhombohedral (M–R) domain boundaries, exhibiting interlayer shear and tensile strain. (a) Schematic of stacking across a domain boundary. Three main bilayer Cr network stacking configurations are shown ( $C2/m$ , boundary, and  $R\bar{3}$  stacking, respectively). From left to right, the teal lattice translates left downward (zigzag direction), whereas the orange lattice moves downward (armchair direction), completing  $a/3$  length translation from M to R stacking. (b) Atomic-resolution ADF-STEM image showing an M–R boundary in  $\text{CrI}_3$ . The enlarged images of the M and R stacking phases are depicted in the right panel. (c) Enlarged STEM image of the R–M boundary and the corresponding inverse fast Fourier transform (IFFT) image. (d) Lateral shifts of a top layer relative to a lower layer give M–R-type stacking configuration along in-plane armchair and zigzag direction translation. The magnetic order in few-layer  $\text{CrI}_3$  with mixed stackings is depicted in the below panel. Scale bars: (b), 2 nm; (b right), 0.5 nm; and (c), 1 nm.

those in  $\text{CrI}_3$ . For instance, the same  $C2/c$  structure with AFM coupling only accounts for 18% (Figure S1i), the same proportion as for  $P3_112$  phase with the FM state. As expected, the  $\text{CrCl}_3$  prefers  $C2/m$  stacking with a percentage of 55% (Figure S1i), reconfirming the hypothesis of  $C2/m$ -enhanced AFM interlayer exchange in few-layer  $\text{CrCl}_3$ ,<sup>37</sup> consistent with our calculation results (Figure S1j). The elementary composition of the  $\text{CrCl}_3$  sample was verified by EDS and EELS (Figure S5g,h).

Besides, multiple stacking polytypes have also been assigned to the layered  $\alpha\text{-RuCl}_3$ , whose elementary composition was confirmed by EDS and EELS (Figure 6g,h). Consistently, we found 11%  $C2/c$  stacking polytypes in few-layer  $\alpha\text{-RuCl}_3$  crystals (Figure 6a,d). As shown in Figure 6,  $C2/m$  (Figure 6b,e) and  $P3_112$  (Figure 6c,f) polytypes are also present in  $\alpha\text{-RuCl}_3$  with a percentage of 14 and 37%, respectively. The results are similar to  $\text{CrCl}_3$  but with a preferred FM  $P3_112$  stacking (Figure 6i,j), reported recently in the  $\alpha\text{-RuCl}_3$  thin film.<sup>39</sup> Because of the relatively smaller atomic number of Cl ( $Z = 17$ ) atoms compared to Ru ( $Z = 44$ ) atoms, the signature striped topologies in the  $C2/c$  and  $C2/m$  phases are more pronounced compared to those in  $\text{CrI}_3$ . Based on our DFT results,  $C2/m$  and  $C2/c$  phases adopt AFM interlayer exchange couplings except in  $\text{CrBr}_3$ , which is always FM regardless of stacking orders, as shown in Table 1. However,  $P3_112$  and  $R\bar{3}$

stackings exhibit completely different magnetic properties in  $\text{MX}_3$  (Figures 3b, S1j, and 6j). Surprisingly, we found that  $C2/c$  and  $C2/m$  inversion structures in  $\text{CrCl}_3$  and  $\text{RuCl}_3$  tend to be FM and ferrimagnetic (FerriM) interlayer couplings, respectively (Table 1).

Interestingly, regardless of the  $\text{MX}_3$  crystals produced by chemical vapor transport (CVT) or purchased from commercial products,  $\text{CrBr}_3$  is almost pure  $R\bar{3}$  phase and mixed phases often occur in  $\text{CrCl}_3$ , whereas other novel structures existing in all of the  $\text{MX}_3$  are waiting for exploration especially in  $\alpha\text{-RuCl}_3$ , as depicted in Figure S13. Furthermore, metal nanoparticles are observed by electron beam reduction from Ru(III) ions, similar to previous observation.<sup>39</sup>

Our atomic-scale STEM results provide direct evidence that various stacking polytypes can exist in few-layer  $\text{MX}_3$  flakes. The distinct magnetic ground states of  $\text{MX}_3$  polytypes demonstrate an effective way to modulate the 2D magnetism via changing the stacking sequences.<sup>6</sup> Furthermore, the AFM interlayer exchange could be broken by changing the stacking sequence to FM/FerriM  $C2/c$ - and  $C2/m$ - inversion symmetry in  $\text{MX}_3$ . The multiple structures provide insights into understanding different ground states in ultrathin  $\text{CrI}_3$  films, which also give clues for the mystery of phase transitions. The multiple phases may suppress the  $C2/m$  to  $R\bar{3}$  (AFM to FM)

transformation when the layer number of  $\text{MX}_3$  is reduced to atomically thin.

### Strain Soliton Boundaries Induced Phase Transition.

When one stacking polytype translates into another, this is usually accompanied by a strain soliton boundary, which creates nontrivial magnetic or electronic states,<sup>49,50</sup> as shown in Figure 7. It can be clearly seen that the stacking order transition from the rhombohedral (R) sequence (upper region) to the monoclinic (M) sequence (lower region) is gradually accommodated by strain soliton boundaries (Figure 7b). The layer stacking in the R phase is illustrated by periodic dark spot arrangement while that in the M sequence is the signature stripy topology (Figure 7b). Toward the top and bottom sides of the STEM image (Figure 7c), the periodic bright spot arrangement represents the stacked  $\text{C2/m}$  and  $\text{R}\bar{3}$  crystals. The brightness decreases at the center of the boundary, and the hexagonal patterns evolve into linear features along the  $(33\bar{1})$  plane of the  $\text{C2/m}$  structure (Figure 7c). Thus, the symmetry is broken as the stacking changes across the boundary, which is always accompanied by the formation of large strain gradients (Figure S14). However, the measurement of  $(33\bar{1})$  interplane distance at the boundary region shows no change compared to that of the R and M phase (Figure 7c), indicating that the transition from R to M can be achieved solely through the shear force along the  $(33\bar{1})$  plane (Figure S14). The high-density dislocations in  $\text{MX}_3$  suggest that the stacking transition is likely intrinsic, which is universal to vdW materials with weak interlayer coupling, resulting in the local interlayer gliding on one side of the boundary and the creation of discrete stacking domains (Figure S1).<sup>51</sup>

A schematic of stacking across the R/M boundary exhibiting shear and tensile strain is shown in Figure 7a. Based on our observations and calculation (Figure S15), we present the following picture to describe the magnetic configurations in few-layer  $\text{CrI}_3$ , as displayed in Figure 7d, describing the coupling of the magnetic response to the stacking order. Inside the R/M boundary, the spin slip passes through a region to complete an interlayer AFM to FM transition (Figure S15). It is known that the magnetic ground state of few-layer  $\text{CrI}_3$  is highly dependent on the stacking order<sup>26,31</sup> and strain.<sup>47</sup> Therefore, this observation provides the opportunity to unveil the complexities of the magnetism of this compound where a structural phase fails to be captured. For instance, the gap between AFM coupling in thin layers ( $\text{C2/c}$  and  $\text{C2/m}$ ) and FM in bulk ( $\text{R}\bar{3}$ ) can be compensated by increasing the proportion of the R phase. As the layer number increases, the accumulated strain soliton boundaries contribute to the density of the R phase, which retain a FM order at a low temperature.<sup>30,37</sup> Together with inversion structures,<sup>52</sup> the relatively thick flakes tend to be FM couplings at the low temperature. In light of our findings, it is not surprising that diverse magnetic orders can coexist in the same flake because each flake can have different amounts of various types of stacking order.

## CONCLUSIONS

In summary, we demonstrated a robust dry transfer method to transfer air-sensitive few-layer  $\text{MX}_3$  for the atomic-resolution electron microscopy study. We systematically analyzed the polytypes in a library of  $\text{MX}_3$ , which provides a comprehensive picture of the magnetism in  $\text{MX}_3$  and points to the possibility of engineering magnetic heterostructures and textures within

the same material by interlayer vdW coupling. Our observations illustrate that the newly discovered  $\text{C2/c}$  monoclinic stacking with well-defined  $\text{C2/m}$  or  $\text{P3}_1\text{12}$  is predominant in several few-layer  $\text{MX}_3$  and is responsible for their 2D magnetism. Besides, a high density of strain soliton boundaries, together with phase distributions determined by stacking energy including potentially the inverted structures of  $\text{C2/c}$  and  $\text{C2/m}$ , would contribute to the AFM–FM transition in few-layer  $\text{MX}_3$ . These results provide useful insights into the complex magnetic behavior in atomically thin  $\text{CrI}_3$  and also clues to designing magnetic phases and developing new functionalities in 2D magnets *via* stacking engineering.

## EXPERIMENTAL SECTION

**Sample Preparation.** The atomically thin  $\text{MX}_3$  flakes were exfoliated from bulk crystals produced by the CVT method<sup>8</sup> or from the commercial products ( $\text{CrI}_3$  and  $\text{CrBr}_3$  are commercial products,  $\text{RuCl}_3$  and  $\text{CrCl}_3$  are from both) and then transferred to the STEM substrate (Cu Quantifoil grid) by a dry transfer technique for STEM observation. Specially, the atomically thin  $\text{MX}_3$  flakes were exfoliated on PDMS stamps,  $\text{MX}_3$  flakes were contacted with the target STEM substrate, and then the PDMS was peeled from the substrate by mild heating. During the transfer process, no chemical etchants nor water is applied. Low-magnification STEM image (Figure S1), EDS, and EELS verified that the as-exfoliated atomically thin  $\text{MX}_3$  flakes were composed of M and X, with the chemical stoichiometry agreeing very well with  $\text{MX}_3$  (Figures 2i,j; 4e,f; 5g,h; and 6g,h).

**ADF-STEM Imaging, Processing, and Simulation.** Atomic-resolution ADF-STEM imaging was performed on an aberration-corrected Nion U-HERMES200 microscope, equipped with a cold field-emission gun operating at 60 kV. The convergence semiangle of the probe was around 35 mrad. Image simulations were performed with the Prismatic package, assuming an aberration-free probe with a probe size of approximately 1 Å. The convergence semiangle and accelerating voltage were in line with the experiments. The collection angle for ADF imaging was between 80 and 200 mrad. ADF-STEM images were filtered by Gaussian filters, and the positions of atomic columns were located by finding the local maxima of the filtered series. The EDS and EELS were collected and processed in a JEOL ARM200F at 80 kV.

**DFT Calculations.** Our first-principles calculations were based on density functional theory (DFT) as implemented in the Vienna *Ab initio* Simulation Package (VASP),<sup>53</sup> using the projector augmented-wave method.<sup>54</sup> The generalized gradient approximation (GGA) with the Perdew–Burke–Ernzerhof<sup>55</sup> realization was adopted for the exchange–correlation functional. We set the on-site effective Hubbard interaction as  $U = 4$  eV (2 eV) in considering the electron correlation of 3d (4d) electrons of Cr (Ru) atoms. The plane-wave cutoff energy was set to 450 eV. A Monkhorst–Pack  $k$ -point mesh<sup>56</sup> with a size of  $9 \times 9 \times 2$  was used for the Brillouin zone sampling. The crystal structure was optimized until the forces on the ions were less than 0.01 eV/Å, and the total energy was converged to  $10^{-5}$  eV with the Gaussian smearing method. The zero-damping DFT-D3 method was adopted to describe the interlayer van der Waals interaction.

## ASSOCIATED CONTENT

### Supporting Information

The Supporting Information is available free of charge at <https://pubs.acs.org/doi/10.1021/jacs.2c12801>.

Figures showing the geometrical and electronic structure differences between various stacking polytypes of  $\text{MX}_3$  (PDF)



## AUTHOR INFORMATION

## Corresponding Authors

Kian Ping Loh – Department of Applied Physics, The Hong Kong Polytechnic University, Hung Hom, Hong Kong SAR 999077, China; Email: [kploh@polyu.edu.hk](mailto:kploh@polyu.edu.hk)

Xiaoxu Zhao – School of Materials Science and Engineering, Peking University, Beijing 100871, China; [orcid.org/0000-0001-9746-3770](https://orcid.org/0000-0001-9746-3770); Email: [xiaoxuzhao@pku.edu.cn](mailto:xiaoxuzhao@pku.edu.cn)

## Authors

Xiaocang Han – School of Materials Science and Engineering, Peking University, Beijing 100871, China

Jing-Yang You – Department of Physics, National University of Singapore, 117551, Singapore; [orcid.org/0000-0003-4559-6592](https://orcid.org/0000-0003-4559-6592)

Shengqiang Wu – School of Materials Science and Engineering, Peking University, Beijing 100871, China

Runlai Li – College of Polymer Science & Engineering, State Key Laboratory of Polymer Materials Engineering, Sichuan University, Chengdu 610065, China

Yuan Ping Feng – Department of Physics, National University of Singapore, 117551, Singapore; [orcid.org/0000-0003-2190-2284](https://orcid.org/0000-0003-2190-2284)

Complete contact information is available at:

<https://pubs.acs.org/10.1021/jacs.2c12801>

## Author Contributions

<sup>†</sup>X.H. and J.-Y.Y. contributed equally to this work.

## Notes

The authors declare no competing financial interest.

## ACKNOWLEDGMENTS

X.Z. thanks the Peking University startup funding and the National Natural Science Foundation of China (grant no. 52273279). J.-Y.Y. and Y.P.F. are supported by the Ministry of Education, Singapore, under its MOE AcRF Tier 2 grant, MOE2019-T2-2-030. K.P.L. acknowledges Grant P0043063 and Global STEM Professorship of Hong Kong Polytechnic University. The authors thank B. Peng, I. Abdelwahab, Z.J. Zhao, and Y.L. Hou for experimental assistances and helpful discussions.

## REFERENCES

- (1) Gong, C.; Li, L.; Li, Z.; Ji, H.; Stern, A.; Xia, Y.; Cao, T.; Bao, W.; Wang, C.; Wang, Y.; Qiu, Z. Q.; Cava, R. J.; Louie, S. G.; Xia, J.; Zhang, X. Discovery of Intrinsic Ferromagnetism in Two-Dimensional van Der Waals Crystals. *Nature* **2017**, *546*, 265–269.
- (2) Huang, B.; Clark, G.; Navarro-Moratalla, E.; Klein, D. R.; Cheng, R.; Seyler, K. L.; Zhong, D.; Schmidgall, E.; McGuire, M. A.; Cobden, D. H.; Yao, W.; Xiao, D.; Jarillo-Herrero, P.; Xu, X. Layer-Dependent Ferromagnetism in a van Der Waals Crystal down to the Monolayer Limit. *Nature* **2017**, *546*, 270–273.
- (3) Gibertini, M.; Koperski, M.; Morpurgo, A. F.; Novoselov, K. S. Magnetic 2D Materials and Heterostructures. *Nat. Nanotechnol.* **2019**, *14*, 408–419.
- (4) Gong, C.; Zhang, X. Two-Dimensional Magnetic Crystals and Emergent Heterostructure Devices. *Science* **2019**, *363*, No. eaav4450.
- (5) Lei, C.; Chittari, B. L.; Nomura, K.; Banerjee, N.; Jung, J.; Macdonald, A. H. Magnetoelectric Response of Antiferromagnetic CrI<sub>3</sub> Bilayers. *Nano Lett.* **2021**, *21*, 1948–1954.
- (6) Soriano, D.; Katsnelson, M. I.; Fernández-Rossier, J. Magnetic Two-Dimensional Chromium Trihalides: A Theoretical Perspective. *Nano Lett.* **2020**, *20*, 6225–6234.
- (7) Song, T.; Cai, X.; Tu, M. W. Y.; Zhang, X.; Huang, B.; Wilson, N. P.; Seyler, K. L.; Zhu, L.; Taniguchi, T.; Watanabe, K.; McGuire, M. A.; Cobden, D. H.; Xiao, D.; Yao, W.; Xu, X. Giant Tunneling Magnetoresistance in Spin-Filter van Der Waals Heterostructures. *Science* **2018**, *360*, 1214–1218.
- (8) Wang, Z.; Gutiérrez-Lezama, I.; Ubrig, N.; Kroner, M.; Gibertini, M.; Taniguchi, T.; Watanabe, K.; Imamoğlu, A.; Giannini, E.; Morpurgo, A. F. Very Large Tunneling Magnetoresistance in Layered Magnetic Semiconductor CrI<sub>3</sub>. *Nat. Commun.* **2018**, *9*, No. 2516.
- (9) Banerjee, A.; Yan, J.; Knolle, J.; Bridges, C. A.; Stone, M. B.; Lumsden, M. D.; Mandrus, D. G.; Tennant, D. A.; Moessner, R.; Nagler, S. E. Neutron Scattering in the Proximate Quantum Spin Liquid  $\alpha$ -RuCl<sub>3</sub>. *Science* **2017**, *356*, 1055–1059.
- (10) Banerjee, A.; Bridges, C. A.; Yan, J. Q.; Aczel, A. A.; Li, L.; Stone, M. B.; Granroth, G. E.; Lumsden, M. D.; Yiu, Y.; Knolle, J.; Bhattarjee, S.; Kovrizhin, D. L.; Moessner, R.; Tennant, D. A.; Mandrus, D. G.; Nagler, S. E. Proximate Kitaev Quantum Spin Liquid Behaviour in a Honeycomb Magnet. *Nat. Mater.* **2016**, *15*, 733–740.
- (11) Chen, L.; Chung, J. H.; Gao, B.; Chen, T.; Stone, M. B.; Kolesnikov, A. I.; Huang, Q.; Dai, P. Topological Spin Excitations in Honeycomb Ferromagnet CrI<sub>3</sub>. *Phys. Rev. X* **2018**, *8*, No. 041028.
- (12) Lee, I.; Utermohlen, F. G.; Weber, D.; Hwang, K.; Zhang, C.; Van Tol, J.; Goldberger, J. E.; Trivedi, N.; Hammel, P. C. Fundamental Spin Interactions Underlying the Magnetic Anisotropy in the Kitaev Ferromagnet CrI<sub>3</sub>. *Phys. Rev. Lett.* **2020**, *124*, No. 017201.
- (13) Wu, J.; Yao, Y.; Lin, M. L.; Rösner, M.; Du, Z.; Watanabe, K.; Taniguchi, T.; Tan, P. H.; Haas, S.; Wang, H. Spin–Phonon Coupling in Ferromagnetic Monolayer Chromium Tribromide. *Adv. Mater.* **2022**, *34*, No. 2108506.
- (14) Klein, D. R.; MacNeill, D.; Lado, J. L.; Soriano, D.; Navarro-Moratalla, E.; Watanabe, K.; Taniguchi, T.; Manni, S.; Canfield, P.; Fernández-Rossier, J.; Jarillo-Herrero, P. Probing Magnetism in 2D van Der Waals Crystalline Insulators via Electron Tunneling. *Science* **2018**, *360*, 1218–1222.
- (15) Kim, H. H.; Yang, B.; Li, S.; Jiang, S.; Jin, C.; Tao, Z.; Nichols, G.; Sfakakis, F.; Zhong, S.; Li, C.; Tian, S.; Cory, D. G.; Miao, G. X.; Shan, J.; Mak, K. F.; Lei, H.; Sun, K.; Zhao, L.; Tsen, A. W. Evolution of Interlayer and Intralayer Magnetism in Three Atomically Thin Chromium Trihalides. *Proc. Natl. Acad. Sci. U.S.A.* **2019**, *116*, 11131–11136.
- (16) Jiang, S.; Li, L.; Wang, Z.; Shan, J.; Mak, K. F. Spin Tunnel Field-Effect Transistors Based on Two-Dimensional van Der Waals Heterostructures. *Nat. Electron.* **2019**, *2*, 159–163.
- (17) Cardoso, C.; Soriano, D.; García-Martínez, N. A.; Fernández-Rossier, J. Van Der Waals Spin Valves. *Phys. Rev. Lett.* **2018**, *121*, No. 067701.
- (18) Cenker, J.; Huang, B.; Suri, N.; Thijssen, P.; Miller, A.; Song, T.; Taniguchi, T.; Watanabe, K.; McGuire, M. A.; Xiao, D.; Xu, X. Direct Observation of Two-Dimensional Magnons in Atomically Thin CrI<sub>3</sub>. *Nat. Phys.* **2021**, *17*, 20–25.
- (19) Huang, B.; Clark, G.; Klein, D. R.; MacNeill, D.; Navarro-Moratalla, E.; Seyler, K. L.; Wilson, N.; McGuire, M. A.; Cobden, D. H.; Xiao, D.; Yao, W.; Jarillo-Herrero, P.; Xu, X. Electrical Control of 2D Magnetism in Bilayer CrI<sub>3</sub>. *Nat. Nanotechnol.* **2018**, *13*, 544–548.
- (20) Song, T.; Fei, Z.; Yankowitz, M.; Lin, Z.; Jiang, Q.; Hwangbo, K.; Zhang, Q.; Sun, B.; Taniguchi, T.; Watanabe, K.; McGuire, M. A.; Graf, D.; Cao, T.; Chu, J. H.; Cobden, D. H.; Dean, C. R.; Xiao, D.; Xu, X. Switching 2D Magnetic States via Pressure Tuning of Layer Stacking. *Nat. Mater.* **2019**, *18*, 1298–1302.
- (21) Jiang, S.; Li, L.; Wang, Z.; Mak, K. F.; Shan, J. Controlling Magnetism in 2D CrI<sub>3</sub> by Electrostatic Doping. *Nat. Nanotechnol.* **2018**, *13*, 549–553.
- (22) Chen, W.; Sun, Z.; Wang, Z.; Gu, L.; Xu, X.; Wu, S.; Gao, C. Direct Observation of van Der Waals Stacking–Dependent Interlayer Magnetism. *Science* **2019**, *366*, 983–987.
- (23) McGuire, M. A.; Dixit, H.; Cooper, V. R.; Sales, B. C. Coupling of Crystal Structure and Magnetism in the Layered, Ferromagnetic Insulator CrI<sub>3</sub>. *Chem. Mater.* **2015**, *27*, 612–620.

- (24) Xie, H.; Luo, X.; Ye, G.; Ye, Z.; Ge, H.; Sung, S. H.; Rennich, E.; Yan, S.; Fu, Y.; Tian, S.; Lei, H.; Hovden, R.; Sun, K.; He, R.; Zhao, L. Twist Engineering of the Two-Dimensional Magnetism in Double Bilayer Chromium Triiodide Homomorphs. *Nat. Phys.* **2022**, *18*, 30–36.
- (25) Song, T.; Sun, Q. C.; Anderson, E.; Wang, C.; Qian, J.; Taniguchi, T.; Watanabe, K.; McGuire, M. A.; Stöhr, R.; Xiao, D.; Cao, T.; Wrachtrup, J.; Xu, X. Direct Visualization of Magnetic Domains and Moiré Magnetism in Twisted 2D Magnets. *Science* **2021**, *374*, 1140–1144.
- (26) Sivadas, N.; Okamoto, S.; Xu, X.; Fennie, C. J.; Xiao, D. Stacking-Dependent Magnetism in Bilayer CrI<sub>3</sub>. *Nano Lett.* **2018**, *18*, 7658–7664.
- (27) Jiang, P.; Wang, C.; Chen, D.; Zhong, Z.; Yuan, Z.; Lu, Z. Y.; Ji, W. Stacking Tunable Interlayer Magnetism in Bilayer CrI<sub>3</sub>. *Phys. Rev. B* **2019**, *99*, No. 144401.
- (28) Sun, Z.; Yi, Y.; Song, T.; Clark, G.; Huang, B.; Shan, Y.; Wu, S.; Huang, D.; Gao, C.; Chen, Z.; McGuire, M.; Cao, T.; Xiao, D.; Liu, W. T.; Yao, W.; Xu, X.; Wu, S. Giant Nonreciprocal Second-Harmonic Generation from Antiferromagnetic Bilayer CrI<sub>3</sub>. *Nature* **2019**, *572*, 497–501.
- (29) Hamer, M. J.; Hopkinson, D. G.; Clark, N.; Zhou, M.; Wang, W.; Zou, Y.; Kelly, D. J.; Bointon, T. H.; Haigh, S. J.; Gorbachev, R. V. Atomic Resolution Imaging of CrBr<sub>3</sub> Using Adhesion-Enhanced Grids. *Nano Lett.* **2020**, *20*, 6582–6589.
- (30) Ray, A.; Shao, Y.-T.; Xu, Y.; Sivadas, N.; Li, T.; Wang, Z.; Mak, K. F.; Shan, J.; Fennie, C.; Muller, D. Mapping Stacking and Stacking Defects in the 2D Ferromagnet CrI<sub>3</sub>. *Microsc. Microanal.* **2020**, *26*, 636–638.
- (31) Thiel, L.; Wang, Z.; Tschudin, M. A.; Rohner, D.; Gutiérrez-Lezama, I.; Ubrig, N.; Gibertini, M.; Giannini, E.; Morpurgo, A. F.; Maletinsky, P. Probing Magnetism in 2D Materials at the Nanoscale with Single-Spin Microscopy. *Science* **2019**, *364*, 973–976.
- (32) Soriano, D.; Cardoso, C.; Fernández-Rossier, J. Interplay between Interlayer Exchange and Stacking in CrI<sub>3</sub> Bilayers. *Solid State Commun.* **2019**, *299*, No. 113662.
- (33) Jang, S. W.; Jeong, M. Y.; Yoon, H.; Ryee, S.; Han, M. J. Microscopic Understanding of Magnetic Interactions in Bilayer CrI<sub>3</sub>. *Phys. Rev. Mater.* **2019**, *3*, No. 031001(R).
- (34) Tsubokawa, I. On the Magnetic Properties of a CrBr<sub>3</sub> Single Crystal. *J. Phys. Soc. Jpn.* **1960**, *15*, 1664–1668.
- (35) Cable, J. W.; Wilkinson, M. K.; Wollan, E. O. Neutron Diffraction Investigation of Antiferromagnetism in CrCl<sub>3</sub>. *J. Phys. Chem. Solids* **1961**, *19*, 29–34.
- (36) Morosin, B.; Narath, A. X-Ray Diffraction and Nuclear Quadrupole Resonance Studies of Chromium Trichloride. *J. Chem. Phys.* **1964**, *40*, 1958–1967.
- (37) Klein, D. R.; MacNeill, D.; Song, Q.; Larson, D. T.; Fang, S.; Xu, M.; Ribeiro, R. A.; Canfield, P. C.; Kaxiras, E.; Comin, R.; Jarillo-Herrero, P. Enhancement of Interlayer Exchange in an Ultrathin Two-Dimensional Magnet. *Nat. Phys.* **2019**, *15*, 1255–1260.
- (38) Cao, H. B.; Banerjee, A.; Yan, J. Q.; Bridges, C. A.; Lumsden, M. D.; Mandrus, D. G.; Tennant, D. A.; Chakoumakos, B. C.; Nagler, S. E. Low-Temperature Crystal and Magnetic Structure of  $\alpha$ -RuCl<sub>3</sub>. *Phys. Rev. B* **2016**, *93*, No. 134423.
- (39) Ziatdinov, M.; Banerjee, A.; Maksov, A.; Berlijn, T.; Zhou, W.; Cao, H. B.; Yan, J. Q.; Bridges, C. A.; Mandrus, D. G.; Nagler, S. E.; Baddorf, A. P.; Kalinin, S. V. Atomic-Scale Observation of Structural and Electronic Orders in the Layered Compound  $\alpha$ -RuCl<sub>3</sub>. *Nat. Commun.* **2016**, *7*, No. 13774.
- (40) Kim, H. S.; Kee, H. Y. Crystal Structure and Magnetism in  $\alpha$ -RuCl<sub>3</sub>: An Ab Initio Study. *Phys. Rev. B* **2016**, *93*, No. 155143.
- (41) Shcherbakov, D.; Stepanov, P.; Weber, D.; Wang, Y.; Hu, J.; Zhu, Y.; Watanabe, K.; Taniguchi, T.; Mao, Z.; Windl, W.; Goldberger, J.; Bockrath, M.; Lau, C. N. Raman Spectroscopy, Photocatalytic Degradation, and Stabilization of Atomically Thin Chromium Tri-Iodide. *Nano Lett.* **2018**, *18*, 4214–4219.
- (42) Castellanos-Gomez, A.; Buscema, M.; Molenaar, R.; Singh, V.; Janssen, L.; Van Der Zant, H. S. J.; Steele, G. A. Deterministic Transfer of Two-Dimensional Materials by All-Dry Viscoelastic Stamping. *2D Mater.* **2014**, *1*, No. 011002.
- (43) Hartel, P.; Rose, H.; Dinges, C. Conditions and Reasons for Incoherent Imaging in STEM. *Ultramicroscopy* **1996**, *63*, 93–114.
- (44) Krivanek, O. L.; Chisholm, M. F.; Nicolosi, V.; Pennycook, T. J.; Corbin, G. J.; Dellby, N.; Murfitt, M. F.; Own, C. S.; Szilagyi, Z. S.; Oxley, M. P.; Pantelides, S. T.; Pennycook, S. J. Atom-by-Atom Structural and Chemical Analysis by Annular Dark-Field Electron Microscopy. *Nature* **2010**, *464*, 571–574.
- (45) Wang, F.; Zhang, Z.; Zhang, Y.; Nie, A.; Zhao, W.; Wang, D.; Huang, F.; Zhai, T. Honeycomb RhI<sub>3</sub> Flakes with High Environmental Stability for Optoelectronics. *Adv. Mater.* **2020**, *32*, No. 2001979.
- (46) Calker, J.; Sivakumar, S.; Xie, K.; Miller, A.; Thijssen, P.; Liu, Z.; Dismukes, A.; Fonseca, J.; Anderson, E.; Zhu, X.; Roy, X.; Xiao, D.; Chu, J. H.; Cao, T.; Xu, X. Reversible Strain-Induced Magnetic Phase Transition in a van Der Waals Magnet. *Nat. Nanotechnol.* **2022**, *17*, 256–261.
- (47) Zhang, Z.; You, J. Y.; Gu, B.; Su, G. Emergent Magnetic States Due to Stacking and Strain in the van Der Waals Magnetic Trilayer CrI<sub>3</sub>. *Phys. Rev. B* **2021**, *104*, No. 174433.
- (48) Kong, X.; Yoon, H.; Han, M. J.; Liang, L. Switching Interlayer Magnetic Order in Bilayer CrI<sub>3</sub> by Stacking Reversal. *Nanoscale* **2021**, *13*, 16172–16181.
- (49) Xu, Y.; Ray, A.; Shao, Y. T.; Jiang, S.; Lee, K.; Weber, D.; Goldberger, J. E.; Watanabe, K.; Taniguchi, T.; Muller, D. A.; Mak, K. F.; Shan, J. Coexisting Ferromagnetic–Antiferromagnetic State in Twisted Bilayer CrI<sub>3</sub>. *Nat. Nanotechnol.* **2022**, *17*, 143–147.
- (50) Hejazi, K.; Luo, Z. X.; Balents, L. Noncollinear Phases in Moiré Magnets. *Proc. Natl. Acad. Sci. U.S.A.* **2020**, *117*, 10721–10726.
- (51) Lin, J.; Fang, W.; Zhou, W.; Lupini, A. R.; Idrobo, J. C.; Kong, J.; Pennycook, S. J.; Pantelides, S. T. AC/AB Stacking Boundaries in Bilayer Graphene. *Nano Lett.* **2013**, *13*, 3262–3268.
- (52) Meseguer-Sánchez, J.; Popescu, C.; García-Muñoz, J. L.; Luetkens, H.; Taniashvili, G.; Navarro-Moratalla, E.; Guguchia, Z.; Santos, E. J. G. Coexistence of Structural and Magnetic Phases in van Der Waals Magnet CrI<sub>3</sub>. *Nat. Commun.* **2021**, *12*, No. 6265.
- (53) Kresse, G.; Furthmüller, J. Efficient Iterative Schemes for Ab Initio Total-Energy Calculations Using a Plane-Wave Basis Set. *Phys. Rev. B: Condens. Matter Mater. Phys.* **1996**, *54*, 11169–11186.
- (54) Blöchl, P. E. Projector Augmented-Wave Method. *Phys. Rev. B* **1994**, *50*, 17953–17979.
- (55) Perdew, J. P.; Burke, K.; Ernzerhof, M. Generalized Gradient Approximation Made Simple. *Phys. Rev. Lett.* **1996**, *77*, 3865–3868.
- (56) Monkhorst, H. J.; Pack, J. D. Special Points for Brillouin-Zone Integrations. *Phys. Rev. B* **1976**, *13*, 5188–5192.